J. Fluid Mech. (2021), *vol*. 913, A45, doi:10.1017/jfm.2020.1167

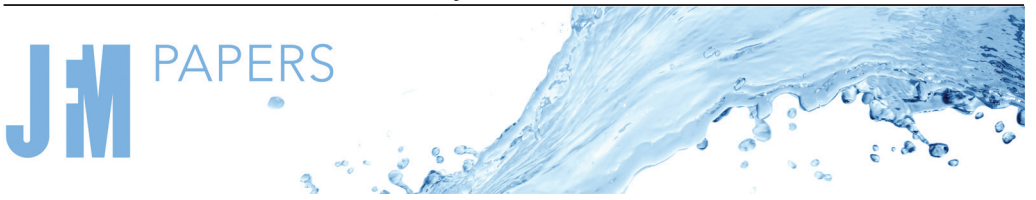

Surface nanodrops and nanobubbles: a classical density functional theory study

Peter Yatsyshin[1],† **and Serafim Kalliadasis**[1]

[1]Department of Chemical Engineering, Imperial College London, London SW7 2AZ, UK

(Received 3 October 2019; revised 16 July 2020; accepted 25 November 2020)

We present a fully microscopic study of the interfacial thermodynamics of nanodrops and nanobubbles, adsorbed on flat substrates with first-order wetting. We show that both nanodrops and nanobubbles are thermodynamically accessible in regions, demarcated by the spinodals of planar wetting films, with nanobubbles occupying a relatively bigger portion of the phase space. While nanodrops can be described as near-spherical caps of Laplace radius, the radius of nanobubbles is very different from the Laplace value. Additionally, nanobubbles are accompanied by a thin gas film adsorbed on the substrate. By computing the interface binding potential, we relate the sphericity of nanodrops to the thin–thick liquid film coexistence (prewetting transition), whereas nanobubble shapes are determined only by the decay of the fluid–substrate forces.

Key words: general fluid mechanics, non-continuum effects

1. Introduction

Sessile drops and bubbles with characteristic dimensions on the nanometre scale play a central role in a wide spectrum of applications, from inkjet printing and vapour–liquid–solid growth processes to micro-/nanofluidics and the design and operation of lab-on-a chip devices. But their theoretical understanding remains incomplete and several fundamental aspects still elude us. This is largely due to the challenging physics of such small objects, often revealing sensitive dependence on the nature of the intermolecular forces, surface wetting properties (Bonn & Ross 2001) and interface fluctuations (Rascón & Parry 2000). In particular, using a model disjoining pressure, Svetovoy *et al.* (2016) recently showed that surface–interface interactions significantly affect the shapes and contact angles of nanobubbles. Recent reviews by Theodorakis & Che (2019), Qian, Arends & Zhang (2019) and Lohse & Zhang (2015) discuss the latest experimental approaches, simulation studies and capillary models of surface nanodrops

† Present address: The Alan Turing Institute, 2QR, 96 Euston Road, London NW1 2DB, UK.
Email address for correspondence: p.yatsyshin@imperial.ac.uk

and nanobubbles. Interesting and promising fully microscopic approaches for computing the disjoining pressure of adsorbed liquid films were recently developed by MacDowell (2011), MacDowell *et al.* (2014) and Nold *et al.* (2014). Using classical density functional theory (DFT), Hughes, Thiele & Archer (2017) and Yin, Sibley & Archer (2019) proposed a method for computing the binding potential which captures the near-wall behaviour of the fluid density. The latter is obtained from a constrained minimisation of the DFT grand free energy functional, subject to an additional requirement that the density profile must have a given thickness of the liquid film.

In the present paper we use DFT to consistently incorporate the existence of the surface phase transitions, particularly the prewetting transition, and uncover their effects on the formation and stability of nanodrops and nanobubbles. This allows us to identify thermodynamic accessibility regions of nanodrops and nanobubbles adsorbed on flat walls. Using DFT we propose a method for computing the interface binding potential, which is based on computing the work of adsorbate formation from the free energy functional. Full unconstrained minimisation of DFT allows us to capture the correct long-ranged asymptotes of the density profiles, which are known to affect the binding potential. It also allows us to treat liquid and gas adsorption consistently within the same framework and uncover a very intriguing relationship between film adsorption and drop/bubble formation.

The intermolecular fluid–fluid and fluid–substrate interactions are considered to be of Lennard–Jones (LJ) type, with potential $\varphi^{6-12}_{\varepsilon,\sigma}(r)$, potential well depth ε and range σ

$$\varphi^{6-12}_{\varepsilon,\sigma}(r) = 4\varepsilon\left[-\left(\frac{\sigma}{r}\right)^6 + \left(\frac{\sigma}{r}\right)^{12}\right], \tag{1.1}$$

where r is the interparticle distance. Such long-range forces typically lead to first-order wetting transitions and planar liquid film coexistence. In the present work we uncover the relations between the intriguing equilibrium properties of nanodrops and nanobubbles and the physics and stability of planar adsorbed wetting films. We stay within the mean-field description of wetting, which remains valid for most practical purposes. The role of interface fluctuations and system dimensionality is discussed, e.g. in excellent reviews by Dietrich (1988) and Saam (2009).

In § 2 we employ a non-local microscopic approach based on DFT. It naturally accounts for the bulk liquid–gas coexistence, planar wetting and the Young contact angle of macroscopic three-phase contact lines, thus fully capturing the physics of nanodrops and nanobubbles. We proceed to discussing the intriguing differences in the microscopic shapes of nanodrops and nanobubbles. We find that adsorbed nanodrops have near-spherical caps of Laplace radius. At the same time, nanobubbles found in the region of the phase diagram which is symmetric with respect to the liquid–gas coexistence line have radii very different from the Laplace value. Additionally, nanobubbles are accompanied by a thin film of gas adsorbed on the substrate. This leads us to relate classical DFT with Derjaguin's approach to wetting in § 3, where we propose a systematic and transferable method for computing the interface binding potential (antiderivative of disjoining pressure) using DFT adsorption isotherms. The binding potential gives us access to the energy landscape of the contact line and reveals that the near sphericity of nanodrops is caused by the remnant of thin–thick liquid film coexistence, the so-called planar prewetting transition. At the same time, the flatter shape of nanobubbles is determined by the absence of such film coexistence during gas adsorption. We summarise our findings in § 4 and provide an outlook of potential broader applications of the fully microscopic route to computing the disjoining pressure.

2. Classical DFT applied to wetting

At any given temperature T and chemical potential μ the equilibrium fluid density $\rho(\boldsymbol{r})$ minimises a grand free energy functional $\Omega[\rho; T, \mu]$, which includes terms describing short-range hard-sphere-like molecular repulsions $F_{hs}[\rho; T]$, long-range attractions $F_{attr}[\rho]$ and the contribution from an external potential $V_{ext}(\boldsymbol{r})$

$$\Omega[\rho\,(\boldsymbol{r})\,; T, \mu] = F_{hs}[\rho; T] + F_{attr}[\rho] + \int V_{ext}(\boldsymbol{r})\rho(\boldsymbol{r})\,\mathrm{d}\boldsymbol{r} - \mu \int \rho(\boldsymbol{r})\,\mathrm{d}\boldsymbol{r}, \tag{2.1}$$

where the integration is carried out over the volume V of the fluid. At equilibrium, (2.1) gives the thermodynamic grand potential $\Omega(T, \mu)$. For a uniform fluid, $\Omega(T, \mu) = -PV$, where P is pressure. Over the years, sophisticated approximations have been developed for each respective contribution in (2.1), see, e.g. the reviews by Evans (1990), Wu & Li (2007) and Lutsko (2010). In the present work we use a simple free energy functional which, despite being minimalistic, still captures the essential physics of the liquid–gas interface near attractive substrates in the LJ model of attractions (Sullivan & Telo da Gama 1986). The intermolecular repulsions are treated within the so-called local density approximation (Pereira & Kalliadasis 2012)

$$F_{hs}\,[\rho\,(\boldsymbol{r})] = \int k_B T \rho(\boldsymbol{r}) \left(\ln\left(\lambda^3 \rho(\boldsymbol{r})\right) - 1\right) \mathrm{d}\boldsymbol{r} + \int \psi(\rho(\boldsymbol{r}))\rho(\boldsymbol{r})\,\mathrm{d}\boldsymbol{r}, \tag{2.2}$$

where k_B is the Boltzmann constant, λ is the de Broglie thermal wavelength and $\psi(\rho)$ is the configurational part of the Carnahan–Starling hard-sphere fluid free energy (Lutsko 2010)

$$\psi(\rho) = k_B T \frac{\eta(4 - 3\eta)}{(1 - \eta)^2}, \quad \eta = \pi\sigma^3\rho/6, \tag{2.3a,b}$$

where σ is the hard-sphere diameter, which here we consider to be fixed and equal to the range of the LJ potential in (1.1). This treatment neglects the weak temperature dependence of the hard-sphere diameter in thermodynamic perturbation theories (Lutsko 2010). The model of $F_{attr}[\rho]$ is the most important DFT ingredient in the present analysis. We use the random phase approximation for the direct correlation function of the uniform LJ fluid

$$F_{attr}\,[\rho\,(\boldsymbol{r})] = \tfrac{1}{2} \int \mathrm{d}\boldsymbol{r} \int \rho\,(\boldsymbol{r})\,\rho\left(\boldsymbol{r}'\right) \varphi_{attr}\left(\left|\boldsymbol{r} - \boldsymbol{r}'\right|\right) \mathrm{d}\boldsymbol{r}', \tag{2.4}$$

where $\varphi_{attr}(r)$ is a mean-field potential

$$\varphi_{attr}\,(r) = \begin{cases} 0, & r \leqslant \sigma \\ \varphi^{6\text{–}12}_{\varepsilon,\sigma}(r), & r > \sigma. \end{cases} \tag{2.5}$$

We are interested in planar adsorption, where the LJ substrate occupies a half-space

$$V_{ext}\,(x) = 4\pi\rho_0\varepsilon_0\sigma_0^3 \left(-\frac{1}{6}\left(\frac{\sigma_0}{H_0 + x}\right)^3 + \frac{1}{45}\left(\frac{\sigma_0}{H_0 + x}\right)^9\right), \tag{2.6}$$

where ρ_0 is the effective substrate density, and ε_0 and σ_0 are the substrate-specific LJ parameters and x is the distance to the wall. We have introduced a low-x cutoff parameter H_0 in (2.6) to eliminate the non-physical divergence of $V(x)$ at fluid–substrate contact. This is a purely mathematical device and does not affect the physics of adsorption as was shown in our earlier work (Yatsyshin & Kalliadasis 2016).

In the present work we investigate the liquid–gas interface and its behaviour near an attractive substrate wall. It is very well known that the physics of the liquid–gas interface is determined by the attractive part of the intermolecular potential (Sullivan & Telo da Gama 1986). This is captured by the mean-field term in (2.4). Although the present DFT model describes the intermolecular attractions in a non-local mean-field fashion, which allows us to consider droplets and bubbles as narrow as several tens of molecular diameters, the intermolecular repulsions are treated by a purely local approximation, as can be seen in the repulsive term in (2.2). This term neglects the excluded volume correlations. As a result, the density profiles we compute do not exhibit the characteristic near-wall oscillations and layering, which can be captured with more refined non-local approximations, such as weighted density or fundamental measure theories (FMT) (Roth 2010), replacing (2.2). However, our DFT given by (2.2) and (2.4) provides a minimalistic valid approximation, which captures all the important physics of the liquid–gas interface and its interplay with the wall in the range of temperatures above the bulk triple point, which we study here. Moreover, we do not expect the molecular packing effects to be important for the qualitative aspects of wetting by liquid above the fluid bulk triple point, for the simple reason that layering transitions do not interfere with prewetting. Similarly, the mean-field nature of our model energy functional implies that our results do not capture effects associated with capillary wave fluctuations. With these shortcomings, our model functional (2.1)–(2.5) provides a suitable microscopic starting point to study the formation of microscopic drops and bubbles. Further discussion of the physical approximations underlying (2.1)–(2.5) and possible approaches to their numerical solution can be found elsewhere (e.g. in Yatsyshin, Savva & Kalliadasis 2015; Yatsyshin, Parry & Kalliadasis 2016; Yatsyshin *et al.* 2017).

The equilibrium density profile $\rho(\boldsymbol{r})$ satisfies the Euler–Lagrange (EL) equation

$$k_B T \ln \rho\left(\boldsymbol{r}\right) + \psi\left(\rho\left(\boldsymbol{r}\right)\right) + \rho\left(\boldsymbol{r}\right) \psi_\rho'\left(\rho\left(\boldsymbol{r}\right)\right) + \int \rho\left(\boldsymbol{r}'\right) \varphi_{attr}\left(\left|\boldsymbol{r}-\boldsymbol{r}'\right|\right) \mathrm{d}\boldsymbol{r}' + V_{ext}\left(\boldsymbol{r}\right) - \mu = 0, \tag{2.7}$$

where $\psi_\rho'(\rho)$ is the derivative of (2.3*a*,*b*) with respect to ρ. In the bulk, $V_{ext}(\boldsymbol{r}) \to 0$ and $\rho(\boldsymbol{r}) \to \rho_b$ (bulk density), and (2.1) and (2.7) give us the pressure and chemical potential

$$P(T, \rho_b) = \rho_b k_B T \frac{1+\eta+\eta^2-\eta^3}{(1-\eta)^3} - \frac{16\pi}{9}\rho_b^2 \sigma^3 \varepsilon, \tag{2.8}$$

$$\mu(T, \rho_b) = k_B T \ln \rho_b + \psi\left(\rho_b\right) + \rho_b \psi_\rho'\left(\rho_b\right) - \frac{32\pi}{9}\rho_b \sigma^3 \varepsilon. \tag{2.9}$$

At bulk liquid–gas coexistence (saturation), $P(T, \rho_l) = P(T, \rho_g) = P_{sat}(T)$ and $\mu(T, \rho_l) = \mu(T, \rho_g) = \mu_{sat}(T)$, where P_{sat} and μ_{sat} are the saturation pressure and chemical potential, respectively. The boundaries of phase metastability are given by the spinodals $\partial P/\partial\rho|_{\rho_g,\rho_l} = 0$; and the critical point at T_c and ρ_c satisfies $\partial P/\partial\rho_c = \partial^2 P/\partial\rho_c^2 = 0$.

In what follows, we adopt a system of units where the hard-sphere diameter σ and the well depth ε in (2.5) are set as units of length and energy, respectively. This leads, e.g. to the bulk critical temperature $T_c = 1.006\varepsilon/k_B$. We also fix the parameters of V_{ext} as $\varepsilon_0 = 0.4$, $\sigma_0 = 2$ and $H_0 = 5$, which gives a first-order wetting wall with a well-defined prewetting line and a relatively high wetting temperature $T_{extw} \approx 0.915$. In bulk metastability regions it is convenient to use the 'disjoining' chemical potential

$\Delta\mu(T) = \mu - \mu_{sat}(T)$. Also, given T and μ, we shall refer to $\Delta\rho(T, \mu) = \rho_b - \tilde{\rho}_b$ as the difference between the densities of phases, stable and metastable in the bulk, respectively. When $\Delta\mu \neq 0$, both ρ_b and $\tilde{\rho}_b$ solve (2.9) at the same T, but $P(T, \rho_b) \geqslant P(T, \tilde{\rho}_b)$.

2.1. *Adsorption of film, drops and bubbles*

Near a planar wall, the fluid density depends on the distance x to the wall. For LJ forces, $\rho(x) - \rho_b = O(x^{-3})$, as $x \to \infty$. Due to the combination of wall–fluid and solvation forces, the wall can adsorb a layer of thickness l of a new phase. For liquid and gas adsorption, the respective $l = l_{liq}$ and $l = l_{gas}$ are given by the same expression, see figure 1(*c*)

$$l(T, \mu) = \frac{\displaystyle\int_0^\infty (\rho(x) - \rho_b)\,\mathrm{d}x}{\Delta\rho(T, \mu)}, \tag{2.10}$$

where $\Gamma(T, \mu) = \int_0^\infty (\rho(x) - \rho_b)\,\mathrm{d}x$ is adsorption. The grand free energy density $\omega(x)$ can be found for $\rho(x)$, at T and μ by rearranging (2.1) (Rowlinson & Widom 1982)

$$\Omega\,[\rho(x); T, \mu] = A\int_0^\infty \omega(x; \rho(x), T, \mu)\,\mathrm{d}x, \tag{2.11}$$

where A is the fluid–wall interface area. The surface tension is given by the integral $\gamma(T) = \int_0^\infty \omega^{ex}(x)\,\mathrm{d}x$, where the excess-over-bulk grand free energy density $\omega^{ex}(x) = \omega(x) + P(\rho_b, T)$, and decays as $O(x^{-3})$ when $x \to \infty$. We can thus compute the surface tensions of the saturated liquid and gas with the wall, γ_{wl} and γ_{wg}, and the surface tension of the free liquid–gas interface γ_{lg}. Off of saturation the Laplace radius of a drop or bubble is $R_L = \gamma_{lg}/\Delta\mu\Delta\rho$ (Rowlinson & Widom 1982; Hauge 1992). At saturation, the Young contact angle $\Theta_Y(T) = \cos^{-1}((\gamma_{wl} - \gamma_{wg})/\gamma_{lg})$ is non-zero below T_w, and vanishes at T_w as $O(\sqrt{T_w - T})$.

Figure 1 represents the mean-field picture of gas and liquid adsorption. The adsorption isotherms $l_{liq}(\mu)$ and $l_{gas}(\mu)$ at $T = 0.88 < T_w$, plotted in figure 1(*a*), represent the bifurcations of two sets of solutions to the EL equation (2.7), $\{\rho(x)\}_T^{gas}$ and $\{\rho(x)\}_T^{liq}$ respectively, with bulk gas and liquid densities. These can be obtained using arc-length continuation, as discussed by Yatsyshin *et al.* (2015). Coloured branches denote (meta)stable surface phases, meaning that the fluid density profiles computed at respective μ are local minima of $\Omega[\rho]$. Grey branches are unstable (respective fluid configurations extremise $\Omega[\rho]$, but are not its minima). Both isotherms diverge at saturation as $O(\Delta\mu^{-1/3})$, when $\Delta\mu \to 0$ from below, where bulk gas is stable and bulk liquid is metastable. In the case of gas adsorption, this is a heterogeneous nucleation of gas, stable in the bulk, on the wall. The unstable branch of the isotherm, where the gas films are thick, corresponds to 'critical' nucleation clusters, and the turning point (spinodal) signals an upward shift of the bulk liquid spinodal, induced by the wall. Below the isotherm spinodal, supersaturated liquid simply cannot coexist with the wall. The liquid adsorption isotherm, on the other hand, represents partial wetting, where the adsorbed liquid is metastable in the bulk. Below T_w, $\Theta_Y > 0$ and thick liquid films are metastable, meaning that their grand potential is higher than that of the thin films at the same μ. Thin–thick film coexistence is a first-order prewetting transition, happening at $T > T_w$ and $\mu = \mu_{pw}(T) < \mu_{sat}$. The unstable branch of the liquid film isotherms, therefore, corresponds to 'critical' prewetting clusters. The isotherm spinodals bound the metastability of thin (green) and thick (red)

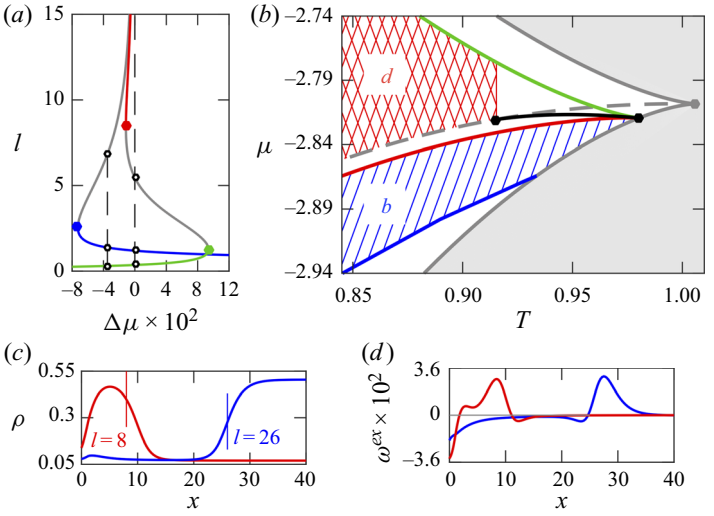

Figure 1. (*a*) Isotherms of liquid and gas adsorption, $l_{liq}(\mu)$ (green-grey-red curve) and $l_{gas}(\mu)$ (blue-grey curve), at $T = 0.88$ ($\Theta_Y = 50.6^\circ$). Grey parts correspond to unstable adsorbed films. Thin liquid films (green) are stable and thick liquid films (red) are metastable. Thin gas films (blue) are stable. Spinodals are designated by filled circles; their T-dependence is shown in (*b*) by respectively coloured lines. Dashed vertical lines at $\Delta\mu = 0$ and $\Delta\mu = -0.035$ are explained in figure 3. (*b*) Bulk coexistence line $\mu_{sat}(T)$ (dashed grey) and its spinodals (solid grey), ending at the critical point (grey circle), $T_c = 1.006$. Metastability is impossible in the grey-shaded region. Prewetting line $\mu_{pw}(T)$ (solid black) starts at $T_w = 0.915$ and ends at $T^c_{pw} = 0.98$ (both are designated by black circles). Surface drops/bubbles occur in the cross-/single-hatched regions, respectively (also designated by '*d*' and '*b*'). (*c*,*d*) Representative profiles of density (with $l = 6$ and $l = 26$, marked in (*c*)) and grand free energy density. Red/blue curves correspond to liquid/gas adsorption.

adsorbed liquid film. The thin film spinodal is a downward shift of the bulk gas spinodal: metastable gas cannot coexist with the wall above it. Notice also that the lower branch of the gas film isotherm is a few molecular diameters higher than its liquid film counterpart. This is a packing effect associated with the solvation force locally repelling the liquid from the wall.

The phase diagram is depicted in figure 1(*b*). At different T, the spinodals of the surface phases (coloured circles in 1*a*) form respectively coloured spinodal lines in 1(*b*). As we shall see, these bound the regions (hatched), where surface drops and bubbles are nucleated on the wall. The bulk liquid–gas coexistence line $\mu_{sat}(T)$ (dashed grey) terminates at the critical point T_c, and bulk spinodals (solid grey) extend tangentially from it, demarcating the metastability regions of bulk liquid (below μ_{sat}) and gas (above μ_{sat}). We reflect the fact that the wall curtails bulk metastability by shading with grey the forbidden region below gas film spinodal and above thick liquid film spinodal, where metastability is impossible. The first-order wetting transition at (T_w, μ_{sat}) marks the coexistence between microscopically thin and macroscopically thick liquid wetting films, and serves as the starting point of the prewetting line $\mu_{pw}(T)$ (black), which approaches saturation tangentially as $\mu_{sat}(T) - \mu_{pw}(T) = O((T - T_w)^{3/2})$, when $T \to T_w$, and terminates at T^c_{pw}, at the prewetting critical point, lying on the bulk gas spinodal. Figures 1(*c*) and 1(*d*) show sample density profiles of adsorbed liquid (red, $l = 8$) and gas (blue, $l = 26$), and the corresponding profiles of excess-over-bulk grand free energy density. Inside adsorbed and bulk phases $\omega^{ex}(x) \approx 0$, and the fluid–wall and liquid–gas interfaces are each associated with an oscillation of $\omega^{ex}(x)$ (blue curves).

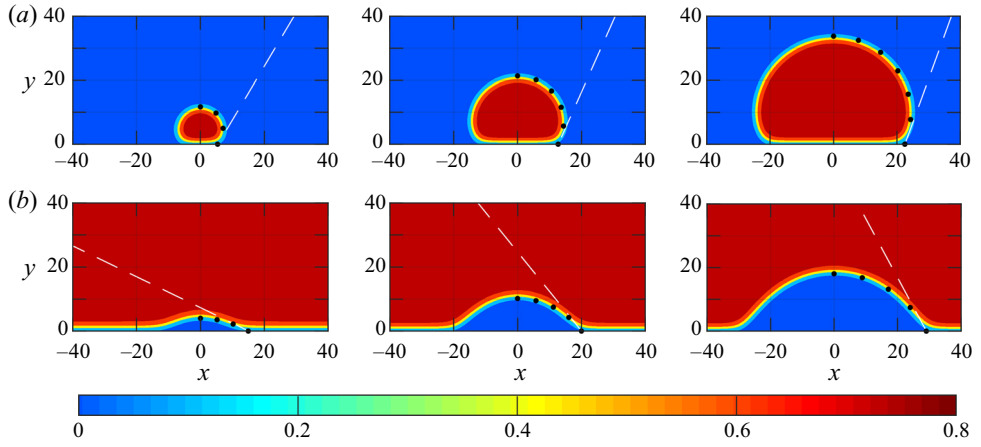

Figure 2. Density profiles of surface nanodrops (a) and nanobubbles (b) at $T = 0.6$ ($\Theta_Y = 105^\circ$), and (left to right) $\Delta\mu = \pm 0.13$ ($R_L \approx 8$), $\Delta\mu = \pm 0.07$ ($R_L \approx 15$), $\Delta\mu = \pm 0.04$ ($R_L \approx 25$), where positive/negative $\Delta\mu$ corresponds to drops/bubbles, respectively. Dotted curves show the arc of a circle, fitted to the liquid–gas interface (density level set at $(\rho_l + \rho_g)/2$) to compute the apparent radii of the drops, $R_d^* \approx 8$, 15, 25 and bubbles, $R_b^* \approx 30$, 25, 32. The apparent contact angles, $\Theta_d^* = 121^\circ$, 114°, 110° and $180^\circ - \Theta_b^* = 154^\circ$, 129°, 118°, are computed by drawing a tangent (dashed lines) to the circular fit at a distance 1σ from the wall. The values of $\Theta_{d/b}^*$ of sufficiently small drops/bubbles are highly sensitive to the technical details of the circle fitting procedure. These values are provided here to illustrate the convergence to Θ_Y as the drop/bubble grows.

Moreover, DFT captures the complicated interplay between these two interfaces at small l (red curves).

On a planar wall, the DFT EL equation (2.7) can only have film-like solutions. To obtain surface drops/bubbles, we insert a nucleation seed by locally increasing/decreasing the potential well of V_{ext} by 5% of its value in 1σ-vicinity of $x = 0$. This perturbation is a purely mathematical device we use to break the symmetry of the EL equation. It does not affect the structure of the adsorbate. A few representative surface drops and bubbles at $T = 0.6 < T_w$ and $|\Delta\mu| \to 0$ are shown in figure 2. Here these configurations are unstable extrema of $\Omega[\rho]$, and thus correspond to critical nucleation clusters of liquid and gas during heterogeneous nucleation on the wall, which acts as the nucleation centre. Indeed, we find that the average inner density inside each drop/bubble is $\rho_b(\mu)$.

The shapes of surface drops and bubbles in figure 2 are affected by several factors. The curvature of the liquid–gas interface leads to the γ_{lg}/R_L pressure increment inside the adsorbed phase. Therefore, the Laplace radius should provide a good overall estimate of the characteristic dimensions of the drops and bubbles. At the same time, the interface shape, especially near the wall, is the result of a complicated interplay between the liquid–gas and wall–fluid interfaces, such as shown in figure 1(d) for flat films. Indeed, near the substrate, the drop interfaces visibly bend in, whilst the bubble interfaces flatten out, connecting with the thin layer of gas, which covers the outside wall and is induced by the solvation force. This is in agreement with the film adsorption isotherms represented in figure 1(a). Moreover, at small and intermediate sizes, bubbles are significantly flatter than the drops. This happens because the ambient phase interacts very strongly with the substrate in the case of bubbles, 'squashing' them.

To test the classical size estimate, given by the Laplace radius, we fit a circle to the liquid–gas interface of surface drops/bubbles and find their 'apparent' radii $R_{d/b}^*$ and

contact angles $\Theta^*_{d/b}$. For figure 2 these are reported in the caption, together with the Laplace radii R_L. We introduced a small near-wall cutoff for fitting the circle to avoid the contribution of the 'flattening' region near the bubble edges.

Let us note that the values of R_L are very close for drops and bubbles at the same $|\Delta\mu|$. This means that a description in terms of R_L, which ignores the microscopic details of fluid–substrate interaction, views drop and bubble adsorption in a completely identical way. Interestingly, for small drops this description seems to hold up, as we see a remarkable agreement between R^*_d and R_L across the drop sizes considered. But the story changes in the case of bubbles where there is hardly any agreement between R_L and the fitted radius of the two smaller bubbles. Clearly, the fluid–substrate interactions neglected by R_L are very important for bubbles. Of course, for larger bubbles R^*_b must start catching up with R_L (and we can see the beginning of this trend between the bubbles with $R^*_b = 25$ and 32), because at saturation the Young contact angle must be recovered. Intuitively, it is clear that the denser liquid above the bubble is attracted to the wall, squashing the bubble. Indeed, this is the intuition behind the binding potential, which we introduce in the next section. This squashing does not happen for drops, because the gas above the drop is too dilute to squash them. We further note that the approach of apparent contact angles to Young values with growing $R^*_{d/b}$ is also clear and is testament to the accuracy of the DFT computation.

Finally, notice that DFT also elegantly reveals the thermodynamics of drop and bubble nucleation, summarised in figure 1(*b*). The wall must be dry to act as a nucleation centre for liquid. Accordingly, we find surface drops forming at $(T < T_w, \mu)$ in the red cross-hatched region of figure 1(*b*). The drop radii are minimal on the liquid film spinodal, and diverge at saturation as $O((P(T, \rho_b) - P_{sat})^{-1})$, according to the Laplace law. Above T_w, $\Theta_Y = 0$ and the wall impurity would nucleate a planar wetting film, see, e.g. Yatsyshin *et al.* (2016, 2017). Surface bubbles can be found in a broader blue-hatched region of figure 1(*b*), above the gas film spinodal, where their radii are minimal. We can still find surface nanobubbles at $T > T_w$ and $\mu < \mu_{sat}$, but as the wall is completely wet at saturation, such bubbles must detach from the surface at sufficiently small $|\Delta\mu|$.

3. Interface binding potential

In this section we introduce a macroscopic description which corrects the spectacular failure of a description in terms of R_L for small bubbles, discussed in the previous section and demonstrated in figure 2. We further relate this revised macroscopic description with DFT and show how the two can be used in tandem to describe small systems with diffuse interfaces, high degree of non-uniformity and highly non-local interactions in terms of the intuitive macroscopic concepts of sharp interfaces and biding potentials.

It is noteworthy that with DFT we did not need to stipulate the existence of interfaces, instead the film-, drop- and bubble-like density configurations with diffuse fluid–fluid and fluid–wall interfaces were obtained by solving the non-local DFT equation (2.7). In fact, the formation of these interfaces is the result of local phase separation, occurring because of the correctly chosen bulk thermodynamic point (T, μ), near bulk coexistence and wall wetting transition. An alternative mean-field approach to wetting can be developed by assuming the existence of a sharp liquid–gas interface, with a shape $l(x)$ minimising the excess free energy functional $\Omega_l[l; T, \mu]$ of the adsorbate at the given T and μ. Here, $l(x)$ is the distance of the liquid–gas interface from the wall. Such a local approach can be traced back to the early works of Frumkin and Derjaguin (FD; see, e.g. Henderson (2011) and references therein). Thus, for a system, translationally invariant along the z-axis, the

interface free energy per unit length can be written in the following general form (see, e.g. Dietrich 1988; Saam 2009)

$$\Omega_l\left[l;T,\mu\right]=\int_{-\infty}^{+\infty}\left[\gamma_{lg}(T)\sqrt{1+\left(\frac{\mathrm{d}l}{\mathrm{d}x}\right)^2}+W\left(l\left(x\right);T,\Delta\mu\right)\right]\mathrm{d}x, \tag{3.1}$$

where the first term of the integrand is the free energy per unit area of the liquid–gas interface, and the second term is the thermodynamic work of adsorbate formation. Depending on whether the adsorbate is formed of liquid or gas, $W\equiv W_{liq}$ or $W\equiv W_{gas}$, respectively, with the corresponding volume and surface contributions

$$W_{liq/gas}\left(l\left(x\right);T,\mu\right)=\Delta\mu\Delta\rho(T,\mu)l\left(x\right)+\gamma_{wl/g}(T)+\gamma_{lg}(T)+g_{liq/gas}\left(l\left(x\right);T\right), \tag{3.2}$$

where $g_{liq/gas}(l;T)$ is the interface binding potential of liquid/gas film, adsorbed at saturation. It accounts for the interatomic interactions between the liquid–gas interface and the substrate. For LJ forces, $g_{liq/gas}(l;T)=O(l^{-2})$, as $l\to\infty$. The EL equation (3.1) becomes

$$\frac{\mathrm{d}^2l}{\mathrm{d}x^2}=\frac{1}{\gamma_{lg}}\left(1+\left(\frac{\mathrm{d}l}{\mathrm{d}x}\right)^2\right)^{3/2}\dot{W}\left(l;T,\mu\right), \tag{3.3}$$

where $\dot{W}(l;T,\mu)$ denotes the derivative of $W(l;T,\mu)$ with respect to l. Equation (3.3) has been referred to as the augmented Young–Laplace equation by Wu & Wong (2004), i.e. the standard Young–Laplace equation modified to include the disjoining pressure. Here, we shall refer to (3.3) as the FD equation because we establish the connection between the microscopic free energy in (2.1) and the macroscopic DF free energy in (3.1), which in turn leads to (3.3). Without consideration of the free energies, this link cannot be established as disjoining pressure is typically associated with the formation of thin films.

If $W(l;T,\mu)$ is known, the FD equation (3.3) can be integrated from the absolute minimum of $W(l;T,\mu)$, until $\mathrm{d}l/\mathrm{d}x$ becomes constant. Notice that, when $\dot{W}\equiv 1$, (3.3) defines a circle of curvature γ_{lg}^{-1}, and when $\dot{W}\equiv 0$, it defines a straight line. Therefore, at μ_{sat} the solution must tend to a flat liquid–gas interface, and below/above μ_{sat}, it must trace a circular-like shape of a drop/bubble. From (3.3), it follows that the curvature of the sharp interface $l(x)$ is given by $\dot{W}/\gamma_{lg}$, where according to (3.2) and the definition of R_L, $\dot{W}\approx\gamma_{lg}/R_L+\dot{g}$. Thus, $\dot{g}/\gamma_{lg}$ has a nice interpretation as the curvature correction to the circular shape of the drop/bubble of Laplace radius, induced by the presence of the substrate.

We can compute the work of film formation $W_{liq}(l;T,\mu)$ and $W_{gas}(l;T,\mu)$ from DFT, using the same density profiles in $\{\rho(x)\}_T^{gas}$ and $\{\rho(x)\}_T^{liq}$ that give rise to the liquid- and gas-adsorption isotherms, such as shown in figure 1(*a*). This requires us to make an ansatz about the density and free energy density profiles of a liquid (or gas) film, of a given height l, adsorbed on the wall at the given T and μ. All we know is that such film must be thermodynamically unstable, unless all three, l, μ and T, belong to a (meta)stable branch of an adsorption isotherm. If we ignore the fact that each profile in the isotherm sets is associated with a particular chemical potential and treat μ as fixed, the sets $\{\rho(x)\}_T^{gas}$ and $\{\rho(x)\}_T^{liq}$ turn out to contain the density profiles of (now unstable) adsorbed films of different widths. Moreover, these density profiles retain the key features of the LJ model of adsorption: a nearly flat plateau at the density of the adsorbed phase, followed by a diffuse liquid–gas interface, consistent with T, and an inverse cubic rate of decay to bulk density.

Also, the near-wall fluid structure and the interaction of the fluid–wall and liquid–gas interfaces at small l are keeping in touch with the underlying DFT functional. Note that since μ is fixed, the large-x limit of the density profiles so chosen do not coincide with the bulk density at μ. This is not a problem, because $W(l;T,\mu)$ is the free energy of the adsorbed film, so the bulk contribution has to be removed anyway. At the same time, the rate of decay of the density profile to its asymptote is important.

Thus, given T, μ and a profile $\rho_0(x)$ from $\{\rho(x)\}_T^{gas}$ or $\{\rho(x)\}_T^{liq}$, which solves the EL equation (2.7) at the required T and some μ_0, we need to compute the height l of the adsorbed film, and its free energy $W(l;T,\mu)$. Associated with $\rho_0(x)$ are its limit $\rho_b^0 = \lim_{x\to\infty}\rho_0(x)$, adsorption $\Gamma_0 = \int_0^\infty(\rho_0(x)-\rho_b^0)\,\mathrm{d}x$, and the grand free energy density $\omega(x;\rho_0(x),T,\mu_0)$, defined in (2.11). It is reasonable to set $l = \Gamma_0/\Delta\rho(T,\mu)$, because then l is related to the physical bulk density (given by T and μ) and correctly recovers $l_0(T,\mu_{sat})$ and $l_0(T,\mu_0)$, see (2.10). Additionally, this ensures that l cannot be 'computed' in the region outside the bulk spinodals, where metastable phases (and thus $\Delta\rho$) do not exit. The free energy of the adsorbed film can be obtained from $\Omega[\rho_0(x);T,\mu]$ in (2.1) by removing the contribution of gas on the outside of the liquid–gas interface. Because the liquid–gas interface is diffuse, simply limiting the integration interval to $[0,l]$ will be incorrect. The solution is to work instead with the grand free energy density, $\omega(x;\rho_0(x),T,\mu_0)$, defined in (2.11). Notice that for large x, $\omega(x;\rho_0(x),T,\mu) = -P(\rho_b^0,T)+(\mu_0-\mu)\rho_b^0 + O(1/x^3)$ as $x\to\infty$. Removing this bulk contribution, we get $W(l;T,\mu)$ by integration

$$\left.\begin{aligned} W(l;T,\mu) &= \int_0^\infty \left[\omega(x;\rho_0,T,\mu) - \left(-P(\rho_b^0,T)+(\mu_0-\mu)\rho_b^0\right)\right]\mathrm{d}x,\\ l &= \int\left(\rho_0(x)-\rho_b^0\right)/\Delta\rho(T,\mu). \end{aligned}\right\} \tag{3.4}$$

Repeating this computation for every profile in $\{\rho(x)\}_T^{gas}$ and $\{\rho(x)\}_T^{liq}$, we tabulate the respective work of gas and liquid film formation, $W^{gas}(l;T,\mu)$ and $W^{liq}(l;T,\mu)$.

In figure 3 we represent the work of film formation at $T=0.85$, and $\Delta\mu=0$ and $\Delta\mu=-0.035$, together with solutions of the FD equation (3.3). The curves $W_{liq}(l;T,\mu)$ (green-grey-red) and $W_{gas}(l;T,\mu)$ (blue-grey), and the FD interfaces $l_{liq}(x)$ and $l_{gas}(x)$, obtained using them, are coloured as the isotherms $l_{liq}(\mu)$ and $l_{gas}(\mu)$ in figure 1(*a*) at respective l. For illustration purposes, we have shifted the curves $l_{gas}(x)$ along the x-axis to facilitate visual comparison with $l_{liq}(x)$. Notice that the unstable parts of $W(l;T,\mu)$ curves (grey) are concave, and separated from the convex stable parts (coloured) by the inflection points (filled circles), which correspond to the spinodals of $l(\mu)$. Local extrema of $W(l;T,\mu)$ (open circles) correspond to the intersections of $l(\mu)$ with lines $\Delta\mu=0$ and $\Delta\mu=-0.035$. In fact, the qualitative behaviour of $W(l;T,\mu)$ and $l(x)$ is apparent from figure 1(*a*): intersections of isotherms with vertical lines $\mu=$ const. must correspond to alternating minima and maxima of $W(l;T,\mu)$.

At saturation (figure 3*a*) the volume contribution to $W(l;T,\mu)$ vanishes, and $W_{liq}(l;T,\mu_{sat})$ and $W_{gas}(l;T,\mu_{sat})$ tend to the respective sums of the liquid–gas and fluid–wall surface tensions, as $l\to\infty$. The inverse quadratic rate of decay of $W_{liq}(l;T,\mu_{sat})$ can be verified numerically, as shown in the inset of figure 3(*a*). Subtracting these asymptotes from $W_{liq}(l;T,\mu_{sat})$ and $W_{gas}(l;T,\mu_{sat})$, would yield the interface binding potential, which turns out to have two branches, associated with liquid and gas adsorption, respectively. The local minima of $W_{liq}(l;T,\mu_{sat})$ at $W_{liq}=\gamma_{wg}$ and that of $W_{gas}(l;T,\mu_{sat})$ at $W_{gas}=\gamma_{wl}$ reflect the fact that when saturation is approached

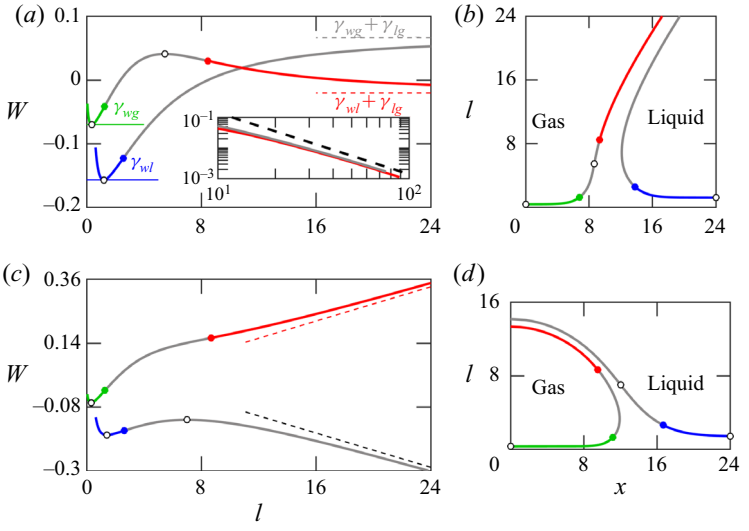

Figure 3. The curve colours and open/filled circles here correspond to those in figure 1(*a*) at the same l. (*a*,*c*) Work of formation of liquid film, $W_{liq}(l;T,\mu)$ (green-grey-red curves), and gas film, $W_{gas}(l;T,\mu)$ (blue-grey curves) at $T=0.88$ ($\Theta_Y=50.6^\circ$). (*b*,*d*) Liquid–gas interfaces, obtained from (3.3) with $W=W_{liq}$ and $W=W_{gas}$, and coloured accordingly. In (*a*,*b*) $\Delta\mu=0$, and in (*c*,*d*) $\Delta\mu=-0.035$. The spinodals of $l(\mu)$ in figure 1(*a*) correspond to the inflection points of W (filled circles), and the intersections of $l(\mu)$ with lines $\Delta\mu=0$ and $\Delta\mu=-0.035$ correspond to the extrema of W (open circles). The asymptotes of W are indicated by dashed lines. In (*a*), the limits and minima of $W(l;T,\mu_{sat})$ are indicated by text; the inset shows the decay of $W(l;T,\mu_{sat})$ on a log–log plot, where the black dashed line is a guide to eye at the expected asymptotic decay $W\propto 1/l^2$.

from the gas/liquid phase, the wall is covered by a stable layer of liquid/gas, respectively (see green/blue branch in figure 1*a*). Since the attractive wall favours liquid, this minimum of $W_{gas}(l;T,\mu_{sat})$ must always be global. On the other hand, the first-order wetting transition brings about a competing minimum of $W_{liq}(l;T,\mu_{sat})$ at $l\to\infty$, which becomes global at $T\geqslant T_w$.

The stability of liquid and gas films, expressed by the work of film formation and, equivalently, by the adsorption isotherms, directly translates into the near-substrate shapes of the liquid–gas interfaces $l(x)$, depicted in figure 3(*b*). At saturation, $l_{liq}(x)$ must have an inflection point at the same l, where $W_{liq}(l;T,\mu_{sat})$ has a local maximum. The existence of such local maximum directly follows from the fact that the binding potential must have two minima to allow for first-order wetting transition. On the other hand, $l_{gas}(x)$ cannot have an inflection point at saturation, because $W_{liq}(l;T,\mu_{sat})$ must monotonically approach $\gamma_{wg}+\gamma_{lg}$ after reaching its local minimum (there is no coexistence between adsorbed gas films). As mentioned above, the starting point on each $l(x)$ is at the minimum of the respective W (marked by open circle), and the numerical solution is stopped when the change of $\mathrm{d}l/\mathrm{d}x$ is below machine tolerance. Since at saturation, $\dot{W}(l)\to 0$ with l as $O(1/l^3)$, $l(x)$ must tend to a straight line with an inclination angle Θ_Y to the x-axis. Numerically we find that Θ_Y, predicted by DFT is reached by $l(x)$ with a remarkable accuracy.

Off of saturation $W(l;T,\mu)$ can be computed by applying (3.4), or from $W(l;T,\mu_{sat})$, by subtracting the volume term $\Delta\mu\Delta\rho l$ and rescaling l appropriately. In figure 3(*c*) we applied (3.4) and verified numerically that $W(l;T,\mu)$ has the linear asymptotes $\Delta\mu\Delta\rho l$ (dashed lines). Notice that here the volume term creates a local maximum for $W_{gas}(l;T,\mu)$

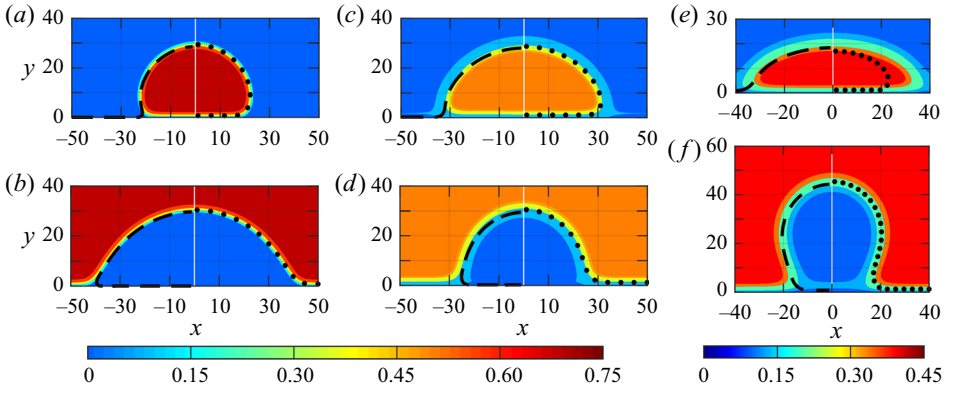

Figure 4. Comparison between DFT (coloured contour plots) and DF model (black curves). In each plot, dashed and dotted black curves to the left and right of the white vertical line at $x = 0$ correspond to $l_{liq}(x)$ and $l_{gas}(x)$, respectively. In (*a–d*) $T < T_w$; the drops and bubbles have the same average height 30σ. In (*e*,*f*) $T > T_w$, and we see a nucleation cluster of the flat prewetting film, and a detaching bubble. Thermodynamic points: (*a*,*b*) $T = 0.65$ ($\Theta_Y = 101^\circ$), $\Delta\mu = -2.4 \times 10^{-2}$ and 3.8×10^{-2}; (*c*,*d*) $T = 0.85$ ($\Theta_Y = 65^\circ$), $\Delta\mu = -1.8 \times 10^{-2}$ and 0.9×10^{-2}; (*d*,*f*) $T = 0.93$ ($\Theta_Y = 0^\circ$, $\Delta\mu_{pw} = -1.4 \times 10^{-3}$), $\Delta\mu = -8.5 \times 10^{-4}$ and -1.0×10^{-2}.

and eliminates it for $W_{liq}(l; T, \mu)$. As a result, the interface line $l_{gas}(x)$ has an inflection point but $l_{liq}(x)$ does not (figure 3*d*). The interface lines must have 'near-circular' shapes when the volume term is non-zero, because if $\dot{W}(l; T, \mu)$ is a constant, (3.3) defines a circle.

The interfaces $l_{liq}(x)$ and $l_{gas}(x)$ differ substantially near the wall, reflecting the fact that the wetting transition and thin–thick film coexistence affects $W_{liq}(l; T, \mu)$, but not $W_{liq}(l; T, \mu)$. Notice also that the effect of the solvation force, locally repelling the liquid from the wall, leads to a higher near-wall part of $l_{gas}(x)$, than $l_{liq}(x)$ in figures 3(*b*) and 3(*c*). The DF model captures this effect via the properly computed work of film formation, where the local minimum of $W_{gas}(l; T, \mu)$ is reached at a slightly higher l, than that of $W_{liq}(l; T, \mu)$. It is noteworthy that the part of $l_{liq}(x)$ between the near-wall region (green) and the outer liquid–gas region (red) is determined by the density profiles $\rho(x)$ from the saddle manifold of $\Omega[\rho(x)]$. Thus, the mean-field DFT functional allows us to connect these metastable states in a non-ambiguous way. In the case of $l_{gas}(x)$, the density profiles from the saddle manifold of $\Omega[\rho(x)]$ determine most of the liquid–gas interface.

In figure 4 we represent a direct comparison between the DFT density profiles and DF interface lines $l_{liq}(x)$ (dashed) and $l_{gas}(x)$ (dotted), obtained at the same T and μ. To superimpose the DF interfaces over $\rho(x, y)$, we aligned the tops of $l_{liq}(x)$ and $l_{gas}(x)$ (where $\mathrm{d}l/\mathrm{d}x$ vanish) with $x = 0$. We also reflected some $l(x)$ with respect to the y-axis, so that $l_{liq}(x)$ and $l_{gas}(x)$ appear in $x \leqslant 0$ and $x \geqslant 0$ half-planes of each plot, respectively. In figures 4(*a*)–4(*c*) we show nanodrops and nanobubbles of the same height 30σ at two different temperatures below T_w. Overall, the local DF model captures well the heights of the drops and bubbles, and the changes of the interface curvature at small scales. As can be seen, $\rho(x, y)$ possesses level sets which closely resemble both ρ_{liq} and ρ_{gas}. Interestingly, no part of $l_{liq}(x)$ can be found between the wall and liquid, just as no part of $l_{gas}(x)$ is found between the wall and gas. This is a limitation of the local functional $\Omega_l[l]$, which does not allow $l(x)$ to bifurcate. Another limitation of the DF model, not apparent from figure 4, was already mentioned above: our treatment of repulsions in (2.2) cannot capture the near-wall layering of the fluid density associated with the excluded volume

intermolecular correlations. This is because our DFT functional was chosen specifically to capture the liquid–gas interface, without the unnecessary complications of the finer near-wall details, which are irrelevant for the present study. Investigating the low-temperature regime, where the near-wall layering is important certainly presents interesting questions for further study, beyond the scope of the present work.

It is very important to understand that a local model, such as DF cannot in principle be expected to replace a statistical-mechanical method, such as DFT. An excellent example illustrating the tight limits of applicability of local models is provided by the continuous prewetting transition (Yatsyshin *et al.* 2016). Since we have a microscopic drop on a substrate, it must nucleate a thin liquid film at μ_{pw} and $T > T_w$ (see figure 1*a*,*b*). While DFT captures the onset of such prewetting without any problem, the DF model breaks down, because it does not include the interactions between different points on the interface. In figure 4(*e*) we depict a nucleation cluster of the flat prewetting film above T_w. The round edges of the adsorbed liquid structure are deceptive. Fitting a circle to the liquid–gas interface as in figure 2, we get $R^* = 49\sigma$. At the same time, the Laplace radius is $R_L = 225\sigma$, testifying to the fact that what we see is indeed a forming flat film. The work $W_{gas}(l; T, \mu)$ does not include the bi-stability of wetting liquid films, and as a result $l_{gas}(x)$ fails to capture the lateral extent of the film. This failure of $l_{gas}(x)$ near the prewetting transition is systematic in our study and manifests the highest disagreement between the DF and DFT models.

Rather surprisingly, we find a remarkable agreement between the local DF and non-local DFT in the case of a nearly detached nanobubble, shown in figure 4(*e*) (since $\Theta_Y = 0$, the surface bubbles will detach as $\Delta\mu \to 0$). The DF interface lines here are *S*-shaped (although still single valued if treated as functions of y), as are the level sets of $\rho(x, y)$. This is curious, because the local free energy Ω_l does not account for the self-interaction in the liquid–gas interface, and the agreement between DF model and DFT should have broken down. It follows that such *S*-shaped profiles are the consequence of the change of sign of $\dot{W}$ in (3.3), and do not necessarily require including curvature and self-interaction effects into the interfacial free energy Ω_l.

4. Conclusions

We have presented a statistical-mechanical study of the thermodynamics and interface shapes of surface nanodrops and nanobubbles. The starting point is a DFT framework based on modelling the fluid–fluid and fluid–substrate interactions at the atomic level. For this purpose we adopted the LJ potential (1.1). At the same time, DFT accounts for the non-locality of interatomic interactions, as manifested by the integral EL equation (2.7) for the fluid density profiles. Because the thermodynamics of liquid–gas coexistence is fully incorporated in DFT, we did not need to assume the existence of fluid–fluid or fluid–wall interfaces as is often the case with macroscopic models of wetting. Given the right thermodynamic point (T, μ) near both bulk coexistence and wall wetting transition, diffuse interfaces appear naturally, as a result of local phase separation. We found that the regions in the thermodynamic space of temperature and chemical potential where nanodrops and nanobubbles exist are demarcated by the spinodals of planar wetting films. Remarkably, this implies that surface nanobubbles may be more amenable to experimental study than nanodrops, precisely because they occupy a bigger portion of the phase plane. Additionally the thin film spinodals can be used to compute the minimal radii of surface drops and bubbles.

Although valuable insight into the contact line region can be gained from microscopic DFT computations, large drops and bubbles are computationally expensive with DFT.

On the other hand, DFT computations clearly show that small bubbles are not spherical caps, and descriptions relying on macroscopic concepts, such as sharp interfaces, contact angles and binding potential, need to appreciate this fact. We provided an example in terms of a simple DF model, which manages to capture the intricate and subtle aspects of non-sphericity of the nanodrop/bubble shapes by accounting for the binding potential. Furthermore, we demonstrated how the binding potential can be related to the much more consistent statistical-mechanical treatment of nanodrops/bubbles with DFT. The method of computing the interface binding potential by renormalising the DFT isotherms is certainly promising in a broader context, e.g. as parameter passing between microscopic statistical-mechanical approaches and continuum mechanical treatments, such as long wavelength approximation to the Navier–Stokes equations. Our results for the binding potential further highlight the important role played by planar wetting in the physics of surface drops and bubbles. For example, from figure 1(*a*) it follows that above the thin film spinodal, $W_{liq}(l; T, \mu)$ will not have a local minimum. Thus, although the Laplace radii are non-zero above the thin film spinodal, the wall wetting mechanism does not allow the drops to form.

Very interestingly, applying the binding potential to compute the contact line of macroscopic drops we find two possible behaviours, depending on whether liquid–gas coexistence is reached from the liquid or gas sides of the phase diagram. Usually, $g(l; T)$ is associated with a liquid film. However, from figure 3(*a*) if follows that $g(l; T)$ must be multivalued, consisting of two (disconnected) branches, corresponding to adsorption of liquid and gas. Of course, in a purely equilibrium setting only one of the configurations $l_{liq}(x)$ is to be observed, because $l_{gas}(x)$ will have a higher free energy, due to the wall favouring liquid. Nevertheless, in a dynamic setting, such as droplet spreading (Kirkinis & Davis 2013; Engelnkemper & Thiele 2019), the metastable states $l_{gas}(x)$ may be manifested as contact line hysteresis. Additionally, introducing a sizable impurity into the substrate, may make $l_{gas}(x)$ the global minimiser of the interfacial free energy.

In our computations, the bulk phase is metastable. This should be viewed as a necessary restriction of the model and may be revisited by investigating pinned drops and bubbles, which will be thermodynamically stable. Another restriction of the present approach is inherent in its mean-field nature, in that interface fluctuations are not accounted for. Nevertheless, far from criticality, mean field is known to provide reliable predictions for most practically interesting cases.

There is much experimental and theoretical interest in understanding the behaviour of apparent contact angles of small drops/bubbles (Qian *et al.* 2019). Our computations demonstrate that the apparent contact angles, such as those shown in figure 2, are highly sensitive to the details of the definition of a sharp interface, as well as the fitting procedure. One needs to be very careful when analysing contact angles using simulation or experimental data for small drops/bubbles, and performing relevant statistical sensitivity analysis (Theodorakis & Che 2017). The agreement we get between DFT and the sharp interface model in (3.3) suggests that rather than fitting spherical caps to nanodrops/bubbles, one should probably attempt to fit a model accounting for disjoining pressure effects, such as (3.3). This can be done using modern data analysis techniques.

We note that DFT models for repulsions of higher sophistication than the local density approximation in (2.2) will reveal the same effects we describe in the present work, because these effects are caused by the molecular attractions and are captured by the random phase approximation for the attractive free energy in (2.4). Nevertheless, more sophisticated repulsive DFT functionals, such as FMT, will facilitate the study of additional effects, associated with excluded volume molecular interactions and

correlations, and the resulting short-ranged near-wall layering of the density profiles at distances of 1–5 molecular diameters from the wall. One of our key findings is that the prewetting transition enables stabilisation of drops of liquid on vanishingly small impurities on the substrate. Certainly, this prompts the existence of a similar relation for low-temperature layering transitions. Investigating these effects is certainly of interest in future work and requires using a repulsive functional with a fully non-local treatment of repulsions. In addition to the effects shown here for molecular attractions, there may appear new minima of the binding potential at low temperatures, associated with the layering transitions and the higher role of molecular repulsions. This will certainly enrich the picture of adsorption presented and could potentially form a very promising direction for future work.

Acknowledgements. We are indebted to Professors A.J. Archer, A.O. Parry and former group member Dr M. Durán-Olivencia for numerous stimulating discussions.

Funding. We acknowledge financial support from the European Research Council via Advanced Grant No. 247031 and from EPSRC via Grant Nos. EP/L020564, EP/L027186/1 and EP/K503733 (EPSRC-Imperial College Pathways to Impact-Impact Acceleration Award).

Declaration of interests. The authors report no conflict of interest.

Author ORCIDs.
Peter Yatsyshin https://orcid.org/0000-0002-8844-281X;
Serafim Kalliadasis https://orcid.org/0000-0001-9858-3504.

References

Bonn, D. & Ross, D. 2001 Wetting transitions. *Rep. Prog. Phys.* **64**, 1085–1163.

Dietrich, S. 1988 Wetting phenomena. In *Phase Transitions and Critical Phenomena* (ed. C. Domb & J.L. Lebowitz), vol. 12. Academic Press.

Engelnkemper, S. & Thiele, U. 2019 The collective behaviour of ensembles of condensing liquid drops on heterogeneous inclined substrates. *Europhys. Lett.* **127**, 54002.

Evans, R. 1990 Microscopic theories of simple fluids and their interfaces. In *Les Houches 1988. Liquids at Interfaces* (ed. J. Charvolin, J.F. Joanny & J. Zinn-Justin), p. 1. North-Holland.

Hauge, E.H. 1992 Macroscopic theory of wetting in a wedge. *Phys. Rev.* A **46**, 4994–4998.

Henderson, D. 2011 Disjoining pressure of planar adsorbed films. *Eur. Phys. J.: Spec. Top.* **197**, 115.

Hughes, A.P., Thiele, U. & Archer, A.J. 2017 Influence of the fluid structure on the binding potential: comparing liquid drop profiles from density functional theory with results from mesoscopic theory. *J. Chem. Phys.* **146** (6), 064705.

Kirkinis, E. & Davis, S.H. 2013 Hydrodynamic theory of liquid slippage on a solid substrate near a moving contact line. *Phys. Rev. Lett.* **110**, 234503.

Lohse, D. & Zhang, X. 2015 Surface nanobubbles and nanodroplets. *Rev. Mod. Phys.* **87**, 981–1035.

Lutsko, J.F. 2010 Recent developments in classical density functional theory. In *Advances in Chemical Physics* (ed. Stuart A. Rice), vol. 144, pp. 1–92. John Wiley & Sons.

MacDowell, L.G. 2011 Computer simulation of interface potentials: towards a first principle description of complex interfaces? *Eur. Phys. J.: Spec. Top.* **197** (1), 131–145.

MacDowell, L.G., Benet, J., Katcho, N.A. & Palanco, J.M.G. 2014 Disjoining pressure and the film-height-dependent surface tension of thin liquid films: new insight from capillary wave fluctuations. *Adv. Colloid Interface Sci.* **206**, 150–171.

Nold, A., Sibley, D.N., Goddard, B.D. & Kalliadasis, S. 2014 Fluid structure in the immediate vicinity of an equilibrium three-phase contact line and assessment of disjoining pressure models using density functional theory. *Phys. Fluids* **26** (7), 072001.

Pereira, A. & Kalliadasis, S. 2012 Equilibrium gas-liquid-solid contact angle from density-functional theory. *J. Fluid Mech.* **692**, 53–77.

Qian, J., Arends, G.F. & Zhang, X. 2019 Surface nanodroplets: formation, dissolution, and applications. *Langmuir* **35**, 12583–12596.

RASCÓN, C. & PARRY, A.O. 2000 Geometry-dominated fluid adsorption on sculpted solid substrates. *Nature* **407**, 986–989.

ROTH, R. 2010 Fundamental measure theory for hard-sphere mixtures: a review. *J. Phys.: Condens. Matter* **22**, 063102.

ROWLINSON, J.S. & WIDOM, B. 1982 *Molecular Theory of Capillarity*. Dover.

SAAM, W.F. 2009 Wetting, capillary condensation and more. *J. Low Temp. Phys.* **157**, 77–100.

SULLIVAN, D.E. & TELO DA GAMA, M.M. 1986 Wetting transitions and multilayer adsorption at fluid interfaces. In *Fluid Interfacial Phenomena* (ed. C.A. Croxton), p. 45. Wiley.

SVETOVOY, V.B., DEVIC, I., SNOEIJER, J.H. & LOHSE, D. 2016 Effect of disjoining pressure on surface nanobubbles. *Langmuir* **32**, 11188–11196.

THEODORAKIS, P.E. & CHE, Z. 2017 Formation, dissolution and properties of surface nanobubbles. *J. Colloid Interface Sci.* **487**, 123–129.

THEODORAKIS, P.E. & CHE, Z. 2019 Surface nanobubbles: theory, simulation, and experiment. A review. *Adv. Colloid Interface Sci.* **272**, 101995.

WU, J. & LI, Z. 2007 Density-functional theory for complex fluids. *Annu. Rev. Phys. Chem.* **58**, 85–112.

WU, Q. & WONG, H. 2004 A slope-dependent disjoining pressure for non-zero contact angles. *J. Fluid Mech.* **506**, 157–185.

YATSYSHIN, P. & KALLIADASIS, S. 2016 Mean-field phenomenology of wetting in nanogrooves. *Mol. Phys.* **114**, 2688–2699.

YATSYSHIN, P., PARRY, A.O. & KALLIADASIS, S. 2016 Complete prewetting. *J. Phys.: Condens. Matter* **28**, 275001.

YATSYSHIN, P., PARRY, A.O., RASCÓN, C. & KALLIADASIS, S. 2017 Classical density functional study of wetting transitions on nanopatterned surfaces. *J. Phys.: Condens. Matter* **29**, 094001.

YATSYSHIN, P., SAVVA, N. & KALLIADASIS, S. 2015 Density functional study of condensation in capped capillaries. *J. Phys.: Condens. Matter* **27**, 275104.

YIN, H., SIBLEY, D.N. & ARCHER, A.J. 2019 Binding potentials for vapour nanobubbles on surfaces using density functional theory. *J. Phys.: Condens. Matter* **31** (31), 315102.